LETTER

doi:10.1038/nature10769

Reconfigurable self-assembly through chiral control of interfacial tension

Thomas Gibaud[1], Edward Barry[1], Mark J. Zakhary[1], Mir Henglin[1], Andrew Ward[1], Yasheng Yang[1], Cristina Berciu[2], Rudolf Oldenbourg[3], Michael F. Hagan[1], Daniela Nicastro[2], Robert B. Meyer[1] & Zvonimir Dogic[1]

From determining the optical properties of simple molecular crystals to establishing the preferred handedness in highly complex vertebrates, molecular chirality profoundly influences the structural, mechanical and optical properties of both synthetic and biological matter on macroscopic length scales[1,2]. In soft materials such as amphiphilic lipids and liquid crystals, the competition between local chiral interactions and global constraints imposed by the geometry of the self-assembled structures leads to frustration and the assembly of unique materials[3–6]. An example of particular interest is smectic liquid crystals, where the two-dimensional layered geometry cannot support twist and chirality is consequently expelled to the edges in a manner analogous to the expulsion of a magnetic field from superconductors[7–10]. Here we demonstrate a consequence of this geometric frustration that leads to a new design principle for the assembly of chiral molecules. Using a model system of colloidal membranes[11], we show that molecular chirality can control the interfacial tension, an important property of multi-component mixtures. This suggests an analogy between chiral twist, which is expelled to the edges of two-dimensional membranes, and amphiphilic surfactants, which are expelled to oil–water interfaces[12]. As with surfactants, chiral control of interfacial tension drives the formation of many polymorphic assemblages such as twisted ribbons with linear and circular topologies, starfish membranes, and double and triple helices. Tuning molecular chirality *in situ* allows dynamical control of line tension, which powers polymorphic transitions between various chiral structures. These findings outline a general strategy for the assembly of reconfigurable chiral materials that can easily be moved, stretched, attached to one another and transformed between multiple conformational states, thus allowing precise assembly and nanosculpting of highly dynamical and designable materials with complex topologies.

In experiments on chiral self-assembly, we used a two-component mixture consisting of 880-nm-long rod-like fd viruses and the non-adsorbing polymer Dextran. In aqueous suspension, fd viruses alone have purely repulsive interactions[13]. Adding non-adsorbing polymer to a dilute isotropic suspension of fd rods induces attractive interactions by the depletion mechanism and leads to their condensation into colloidal membranes, which are equilibrium structures consisting of one-rod-length-thick, liquid-like monolayers of aligned rods[11] (Fig. 1a). Despite having different structures on molecular length scales, the coarse-grained properties of colloidal membranes are identical to those of conventional lipid bilayers. However, unlike their amphiphilic counterparts, colloidal membranes do not form vesicles and are instead observed as freely suspended disks with exposed edges. Here we investigate the behaviour of these exposed edges in a manner analogous to previously studied liquid–liquid domains embedded in lipid bilayers[14–16]. For our experiments, it is essential that fd viruses are chiral, that is, a pair of aligned viruses minimizes their interaction energy when they are slightly twisted with respect to each other in a preferred direction. The strength of chiral interactions can be continuously tuned to zero through either genetic or physical methods[13,17] (Supplementary Fig. 1).

Before investigating chiral membranes, we determined the edge structure of a membrane composed of simpler, achiral rods using three complementary imaging techniques, namely two-dimensional (2D) and three-dimensional (3D) polarization microscopy and electron microscopy. The local tilting of the rods within a membrane was determined using a 2D LC-PolScope, which produces images in which the intensity of each pixel represents the local retardance of the membrane[18] (Fig. 1d). Such images can be quantitatively related to the tilting of the rods away from the layer normal[19] (the z axis). Rods in the bulk of a membrane are aligned along the z axis, and it follows that 2D LC-PolScope images appear black in that region (Fig. 1e). By contrast, the bright, birefringent ring along the membrane's periphery reveals local tilting of the rods (Fig. 1e and Supplementary Fig. 2). For achiral rods, this indicates that a membrane has a hemi-toroidal curved edge (Fig. 1b, c). By comparison with an untilted edge, a curved edge structure lowers the area of the rod–polymer interface, thus reducing interfacial tension, at the cost of increasing the elastic energy due to a twist distortion. This hypothesis is confirmed by visualizing the 3D membrane structure using electron tomography, which shows that the viruses' long-axis transitions from being parallel to the z axis in the membrane bulk to being perpendicular to the z axis and tangential to the edge along the membrane periphery (Fig. 1d and Supplementary Fig. 3). For achiral viruses, the spontaneous twist at the edges is equally likely to be clockwise or anticlockwise. However, the 2D LC-PolScope records only 2D projections of the birefringence map and thus cannot distinguish between these two possibilities. For this reason, we used a 3D LC-PolScope[20], which reveals that achiral rods are equally likely to tilt in either direction, thus confirming the spontaneously broken chiral symmetry at the edge of an achiral membrane (Fig. 1f–h and Supplementary Fig. 4). Simulations of hard, achiral spherocylinders and depletant molecules provide additional verification that interfacial effects alone cause spontaneous twisting of achiral rods at the membrane's edge (Supplementary Fig. 5).

When viewed with optical microscopy, a membrane's edge shows pronounced thermal fluctuations, the analysis of which yields the line tension, γ_{eff}, which is the energetic cost required to move rods from the membrane interior to the periphery[12,21,22] (Fig. 2a). A typical fluctuation spectrum for an achiral edge is shown in Fig. 2b. In the regime of small wavevector, q, the mean square Fourier amplitudes, $\langle a_q{}^2 \rangle$, are independent of q, allowing us to extract the effective line tension, $\gamma_{\mathrm{eff}} = k_{\mathrm{B}}T/\langle a_q{}^2 \rangle$ (ref. 12), where k_{B} is the Boltzmann constant and T is the temperature. In the large-q limit, fluctuations scale as $1/q^2$ and are therefore substantially suppressed relative to those of a simple interface. One possible explanation is that fluctuations are suppressed as a result of a quasi-one-dimensional (quasi-1D) nematic phase at the edge, which is a direct consequence of rod tilting (Fig. 1e). At large wavelengths, the elastic energy required to deform the quasi-1D nematic phase is negligible and the fluctuations are dominated by the line tension. With decreasing wavelength, there is an increasing energetic penalty associated with bending the quasi-1D nematic phase, resulting in the suppression of fluctuations.

[1]The Martin Fisher School of Physics, Brandeis University, 415 South Street, Waltham, Massachusetts 02454, USA. [2]Department of Biology, Brandeis University, 415 South Street, Waltham, Massachusetts 02454, USA. [3]Marine Biological Laboratory, 7 MBL Street, Woods Hole, Massachusetts 02543, USA.

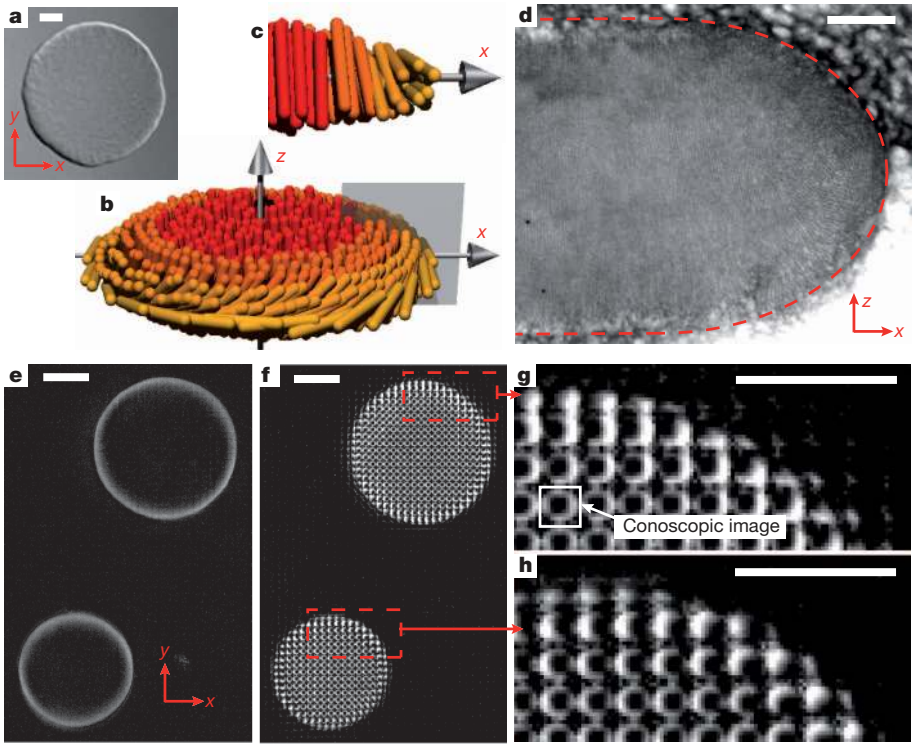

Figure 1 | Edge structure of membranes assembled from an achiral mixture of wild-type and Tyr21Met fd phages. **a**, Differential interference contrast (DIC) image of a colloidal membrane. **b**, Illustration of colloidal membrane indicating that its edge adopts a surface-tension-minimizing curved profile, forcing rods to twist locally. For clarity, the aspect ratio of rods has been reduced. **c**, Cross-section shown in **b**. **d**, Electron micrograph of a membrane directly visualizing the curved edge profile (Supplementary Fig. 3). **e**, 2D LC-PolScope birefringence map of two membranes. The bright band associated with the edges indicates local rod tilting (Supplementary Fig. 2). **f**, 3D LC-PolScope image composed of an array of conoscopic microimages, each sampling the local orientation of the rods. In each microimage, the displacement of the dark spot away from the centre determines the local tilting of the rods with respect to the layer normal (the *z* axis; Supplementary Fig. 4). **g**, **h**, Sections of 3D LC-PolScope images of two edges with clockwise (**g**) and anticlockwise (**h**) twists, respectively, illustrating the broken chiral symmetry found at the edge of achiral membranes. Scale bars, 5 μm (**a**, **e**–**g**, **h**); 0.2 μm (**d**).

Next we demonstrated that the chirality of the constituent rods controls the magnitude of γ_{eff}. The global constraints imposed by the 2D membrane topology are fundamentally incompatible with local twisting (chiral interactions) between constituent rods, leading to the expulsion of chirality from the bulk of the membrane[7] (untwisting of rods). It follows that introducing chirality raises the energy of rods in the membrane bulk while simultaneously lowering the energy of rods close to the edge, where they are free to twist and satisfy chiral interactions. Therefore, we propose that there are two contributions to the effective line tension, γ_{bare} and γ_{chiral}, such that $\gamma_{eff} = \gamma_{bare} - \gamma_{chiral}$, where γ_{bare} is the line tension of a membrane edge composed of achiral rods and γ_{chiral} is the chiral contribution to the line tension[19,23]. To measure γ_{bare} and γ_{chiral} independently, we used the temperature dependence of fd chirality (Supplementary Fig. 1). We measured γ_{bare} at high temperature (60 °C), where rods are achiral ($\gamma_{chiral} = 0$) and, therefore, $\gamma_{eff} = \gamma_{bare}$ (Fig. 2c). Decreasing the temperature increases the strength of chiral interactions, resulting in a smaller γ_{eff} value and demonstrating that chirality indeed reduces line tension (Fig. 2c). Temperature-dependent chiral contributions ($\gamma_{chiral}(T) = -\gamma_{eff}(T) + \gamma_{bare}$) were converted into a function that depends on the chiral wavevector, q_0, using measurements of the temperature dependence of the cholesteric twist (Supplementary Fig. 1). Notably, measurements of γ_{chiral} at different depletant concentrations collapse onto a universal curve (Fig. 2d), confirming that the two contributions to γ_{eff} are uncorrelated. Our data show that chirality can reduce the line tension by as much as $450 k_B T$ per micrometre of edge length (Fig. 2d). To test this hypothesis independently, we measured γ_{eff} for membranes composed of the Tyr21Met mutant fd virus. By contrast with wild-type fd virus, the chirality of this mutant fd virus is temperature independent (Supplementary Fig. 6). We find that γ_{eff} for the Tyr21Met mutant membranes is temperature independent over the entire measurement range, unambiguously demonstrating chiral control of line tension and ruling out any intrinsic temperature effects.

Our findings raise the possibility that at sufficiently low temperatures the chiral contribution to interfacial energy could dominate the bare line tension, lowering the energetic cost of creating edges and leading to

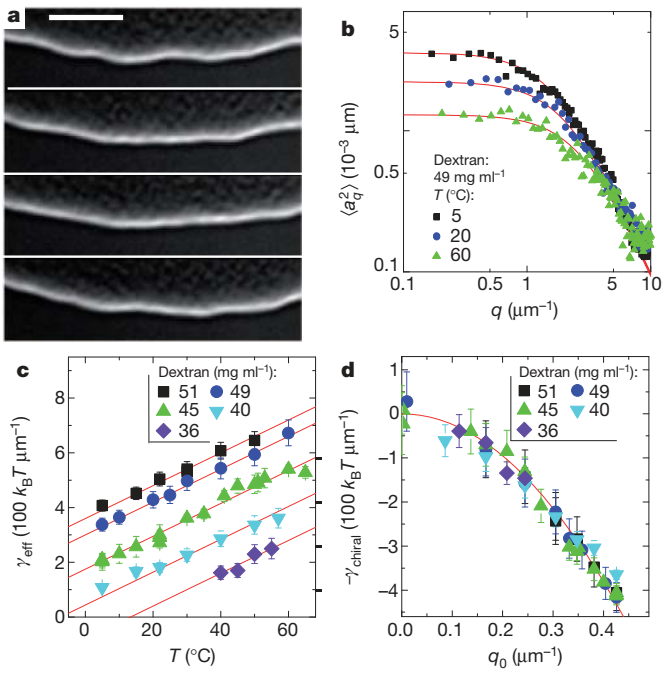

Figure 2 | Chiral control of effective line tension, γ_{eff}. **a**, DIC images, taken 1 s apart, illustrating the fluctuations of the membrane's edge. Scale bar, 5 μm. **b**, Fluctuation spectrum ($\langle a_q^2 \rangle$ versus q) plotted for three different temperatures. For small q, $\langle a_q^2 \rangle$ is independent of q and inversely proportional to the effective line tension, $\gamma_{eff} = k_B T / \langle a_q^2 \rangle$. For large q, the suppressed fluctuations are independent of depletant concentration (osmotic pressure) and sample temperature (fd chirality) and scale as $1/q^2$. Red lines are fits using equation (3) (Methods). **c**, γ_{eff} extracted from the low-q regime, plotted for a range of sample temperatures (fd chirality) and Dextran concentrations (osmotic pressures). In the achiral limit at 60 °C, $\gamma_{chiral} = 0$ and $\gamma_{bare} = \gamma_{eff}$. Increasing the Dextran concentration increases γ_{bare}. Decreasing the temperature reduces γ_{eff} because γ_{chiral} increases. The red lines of fixed slope are guides to the eyes illustrating the universal scaling of γ_{eff} with chirality. **d**, γ_{chiral} as a function of the twist wavevector, q_0 (measured in the cholesteric phase), for various depletant concentrations. The temperature dependence of q_0 is extracted from Supplementary Fig. 1. The red curve is quadratic fit to the data: $\gamma_{chiral} = C q_0^2$. Error bars, s.d.; $n = 10$.

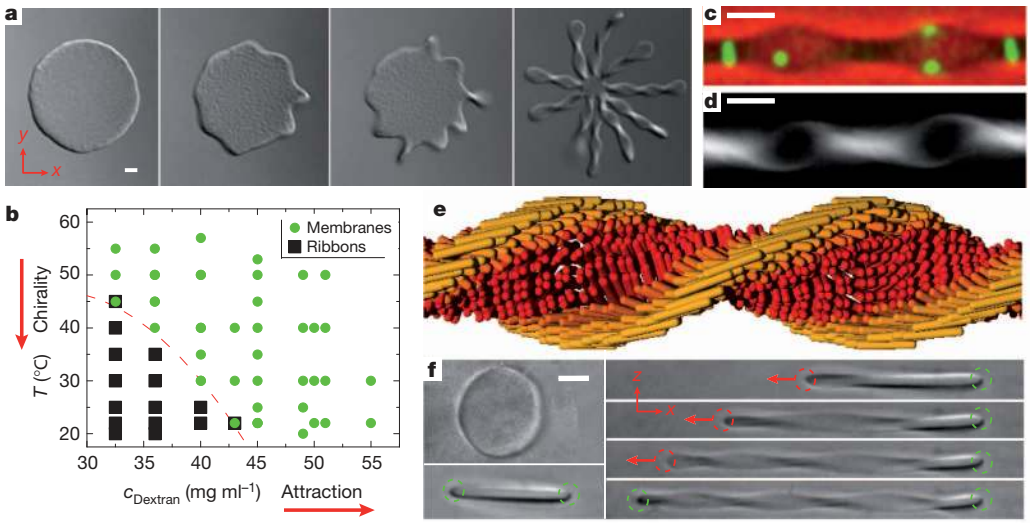

Figure 3 | Transition of a 2D disk into 1D twisted ribbons. **a**, A temperature quench reduces the line tension, inducing a transition of the 2D membrane into 1D twisted ribbons (Supplementary Movie 1). **b**, The stability diagram indicates regions of phase space where ribbons and membranes are observed as a function of temperature (chirality) and Dextran concentration ($c_{Dextran}$). The boundary indicates the temperature above which no stable or metastable ribbons are observed at a given Dextran concentration. **c**, An overlaid phase contrast (red)/fluorescence (green) image of a stable ribbon containing a low volume fraction of fluorescently labelled rods (Supplementary Movie 2). **d**, LC-PolScope image indicating rod tilting that penetrates from the edge of the ribbon towards its centre. The intensity at each pixel is proportional to $\sin^2(\theta)$, where θ is the local rod tilt angle away from the image plane. **e**, Schematic structure of twisted ribbons as deduced from optical microscopy. **f**, A 2D colloidal membrane is trapped with a dual-beam optical trap and stretched, inducing the transition to a 1D twisted ribbon (Supplementary Movie 3). Red circles indicate moving traps and green circles indicate fixed traps. Scale bars, 2 μm.

their spontaneous formation. In this respect, we expect chirality to have a role similar to that of amphiphilic surfactants in oil–water mixtures. Such surfactants lower surface tension and lead to the formation of excess interfaces through the assembly of microemulsions. To investigate this possibility, we quenched a membrane assembled at low depletant (Dextran) concentration from the high-temperature achiral phase. With decreasing temperature, fluctuations of the membrane edge become more pronounced, indicating that γ_{eff} is decreasing. Eventually the edge becomes unstable, resulting in a remarkable polymorphic transition in which twisted, ribbon-like structures grow along the entire periphery of the disk, generating a starfish-shaped membrane (Fig. 3a and Supplementary Movie 1). This polymorphic transition is reversible; with increasing temperature, the starfish membrane collapses back into a disk. The stability diagram indicates that 1D twisted ribbons are stable at low Dextran concentrations and low temperatures (small γ_{bare} values and large γ_{chiral} values), whereas flat 2D membranes are stable for large γ_{bare} values or small γ_{chiral} values (Fig. 3b). DIC microscopy reveals the overall structure of the ribbons, such as their pitch and width (Fig. 3a); fluorescence microscopy shows the liquid-like dynamics of single rods within the assemblage (Fig. 3c and Supplementary Movie 2); and 2D LC-PolScope imaging quantitatively determines the local tilt of the rods (Fig. 3d). A schematic representation of the twisted ribbons based on this information, indicating inhomogeneous tilting of the rods within a ribbon, is shown in Fig. 3e. Such data are in agreement with recent theoretical predictions[24].

Chiral self-assembly produces structures that combine seemingly divergent properties of high elasticity and fluidity. To demonstrate these properties, we trapped two opposite sides of a flat disk with a dual-beam optical trap and applied an extensional force, causing the transition from a stretched disk into a twisted ribbon (Fig. 3f and Supplementary Movie 3). This mechanically induced disk-to-ribbon transition is reversible; on removal of the optical trap, the highly elastic ribbon relaxes back into its original shape. Furthermore, using optical tweezers it is possible to change the architecture of the chiral assemblages systematically, allowing new pathways for assembling nanomaterials with highly complex topologies. For example, two ends of a linear twisted ribbon are easily joined together to assemble a closed, ring-like polymeric structure. The disk-to-ribbon transition is tightly coupled to the assemblage topology (Fig. 4d). On increasing the temperature, all linear ribbons transform into achiral disks (Supplementary Movie 4), whereas closed, ring-like ribbons remain twisted owing to the constraint imposed by the ring topology (Supplementary Movie 5).

The chiral assembly pathways described here are hierarchical, opening up the possibility that simple changes on microscopic (ångström) length scales can be used to control structures on macroscopic (millimetre) length scales[25,26]. At the smallest relevant length scale, each virus is assembled from DNA that is coated with thousands of

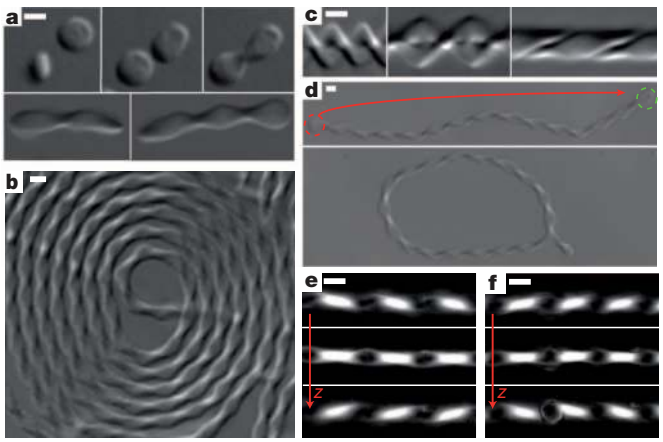

Figure 4 | Hierarchical self-assembly: from isolated viruses and metastable disks to singly and doubly twisted ribbons. **a**, In the ribbon region of the phase diagram in Fig. 3b, fd viruses condense into metastable, self-limited disks. On longer timescales, these disks coalesce and form 1D twisted ribbons. **b**, Image of a single ribbon that has collapsed into a toroid. **c**, Doubly twisted ribbons are assembled by wrapping around each other two singly twisted ribbons with a well-defined phase difference (Supplementary Fig. 8). **d**, Directed assembly of a ring-like supramolecular polymer from a linear twisted ribbon using optical tweezers. **e**, **f**, Single point mutation of the major coat protein permits microscopic control of ribbon chirality. Wild-type fd virus assembles into left-handed ribbons (**e**), whereas the Tyr21Met fd virus forms right-handed ribbons (**f**), as demonstrated by the *z*-stack series of 2D LC-PolScope images. Scale bars, 2 μm.

copies of the major coat protein. At the mesoscopic length scale, attractive depletion interactions condense dilute, rod-like viruses into self-limited, metastable, mesoscopic colloidal disks whose diameter is approximately one twist penetration length[19,23,27,28] (Fig. 4a). Once assembled, mesoscopic disks themselves experience mutual attractions, resulting in lateral coalescence and formation of twisted doublets. On longer timescales, this coalescence process continues, producing ribbons with complex topologies and multiple branching points (Supplementary Fig. 7). The length of these ribbons can reach macroscopic (millimetre) dimensions. This hierarchical assembly process describes a robust synthesis of ribbons that behave as supramolecular polymers and can assemble into even more-complex structures at higher levels of hierarchy, such as toroids (Fig. 4b). Under certain conditions, ribbons also wrap around each other to produce a great variety of double- and triple-helical structures (Fig. 4c and Supplementary Fig. 8). A challenge associated with hierarchical assembly pathways is to control the final macroscopic assemblage by specific modification of relevant microscopic parameters. Previous work showed that even a single amino-acid mutation of the major coat protein can alter the microscopic chirality of individual viruses[13]. We used this finding to demonstrate that such amino-acid exchange propagates across all hierarchical levels, switching the ribbon handedness and allowing for microscopic control of macroscopic ribbon chirality (Fig. 4e, f).

We have shown that the chirality of the constituent molecules can be used to tune the line tension associated with the exposed edge of a colloidal monolayer membrane. The potential of hierarchical chiral self-assembly is demonstrated by assembling reconfigurable materials with unique mechanical properties and complex topologies that can easily switch between multiple polymorphic forms[29,30].

METHODS SUMMARY

Wild-type and Tyr21Met fd viruses were purified according to previously published protocols[13]. To reduce the number of longer viruses, which destabilize monolayer structures such as colloidal membranes or twisted ribbons, virus suspensions were cycled through isotropic–nematic phase coexistence. Only the isotropic portion of the samples, enriched in shorter viruses, was used for experiments[11]. The polydispersity of viruses was quantified using gel electrophoresis (Supplementary Fig. 9). All samples were prepared in a buffer containing 20 mM Tris and 100 mM NaCl at pH 8.0. Addition of the non-adsorbing polymer Dextran (relative molecular mass, 500,000; Sigma-Aldrich) induces condensation of rod-like viruses into either flat colloidal membranes or various other chiral assemblages. The strength of chiral interactions between rods was tuned either by changing the sample temperature or by varying the ratio of wild-type fd virus to Tyr21Met fd virus in membranes containing a mixture of the two[13]. Optical microscopy data was taken with an inverted microscope (Nikon TE-2000) equipped with DIC optics, a homemade heating/cooling stage and a cooled charged-coupled-device camera (QImaging, Retiga Exi). The 2D and 3D LC-PolScope imaging set-ups have been described elsewhere[18,20]. To prevent binding of viruses to surfaces, microscope slides and coverslips were cleaned and subsequently coated with a silane agent (3-(trimethoxysilyl) propyl methacrylate, Sigma Aldrich) to which a polyacrylamide brush was polymerized from methacrylate groups.

Full Methods and any associated references are available in the online version of the paper at www.nature.com/nature.

Received 31 July; accepted 6 December 2011.
Published online 4 January 2012.

1. Pasteur, L. On the relations that can exist between crystalline form, and chemical composition and the sense of rotary polarization. *Ann. Chim. Phys.* **24,** 442–459 (1848).
2. Hirokawa, N., Tanaka, Y., Okada, Y. & Takeda, S. Nodal flow and the generation of left-right asymmetry. *Cell* **125,** 33–45 (2006).
3. Harris, A. B., Kamien, R. D. & Lubensky, T. C. Molecular chirality and chiral parameters. *Rev. Mod. Phys.* **71,** 1745–1757 (1999).
4. Oda, R., Huc, I., Schmutz, M., Candau, S. J. & MacKintosh, F. C. Tuning bilayer twist using chiral counterions. *Nature* **399,** 566–569 (1999).
5. Aggeli, A. *et al.* Hierarchical self-assembly of chiral rod-like molecules as a model for peptide beta-sheet tapes, ribbons, fibrils, and fibers. *Proc. Natl Acad. Sci. USA* **98,** 11857–11862 (2001).
6. Kamien, R. D. & Selinger, J. V. Order and frustration in chiral liquid crystals. *J. Phys. Condens. Matter* **13,** R1–R22 (2001).
7. de Gennes, P. G. An anology between superconductors and smectics A. *Solid State Commun.* **88,** 1039–1042 (1993).
8. Renn, S. R. & Lubensky, T. C. Abrikosov dislocation lattice in a model of the cholesteric to smectic-A transition. *Phys. Rev. A* **38,** 2132–2147 (1988).
9. Matsumoto, E. A., Alexander, G. P. & Kamien, R. D. Helical nanofilaments and the high chirality limit of smectics *A. Phys. Rev. Lett.* **103,** 257804 (2009).
10. Hough, L. E. *et al.* Helical nanofilament phases. *Science* **325,** 456–460 (2009).
11. Barry, E. & Dogic, Z. Entropy driven self-assembly of nonamphiphilic colloidal membranes. *Proc. Natl Acad. Sci. USA* **107,** 10348–10353 (2010).
12. Safran, S. *Statistical Thermodynamics of Surfaces, Interfaces, and Membranes* 79–85 (Addison Wesley, 1994).
13. Barry, E., Beller, D. & Dogic, Z. A model liquid crystalline system based on rodlike viruses with variable chirality and persistence length. *Soft Matter* **5,** 2563–2570 (2009).
14. Baumgart, T., Hess, S. T. & Webb, W. W. Imaging coexisting fluid domains in biomembrane models coupling curvature and line tension. *Nature* **425,** 821–824 (2003).
15. Honerkamp-Smith, A. R. *et al.* Line tensions, correlation lengths, and critical exponents in lipid membranes near critical points. *Biophys. J.* **95,** 236–246 (2008).
16. Lee, K. Y. C. & McConnell, H. M. Quantitized symmetry of liquid monolayer domains. *J. Phys. Chem.* **97,** 9532–9539 (1993).
17. Dogic, Z. & Fraden, S. Cholesteric phase in virus suspensions. *Langmuir* **16,** 7820–7824 (2000).
18. Oldenbourg, R. & Mei, G. New polarized light microscope with precision universal compensator. *J. Microsc.* **180,** 140–147 (1995).
19. Barry, E., Dogic, Z., Meyer, R. B., Pelcovits, R. A. & Oldenbourg, R. Direct measurement of the twist penetration length in a single smectic a layer of colloidal virus particles. *J. Phys. Chem. B* **113,** 3910–3913 (2009).
20. Oldenbourg, R. Polarized light field microscopy: an analytical method using a microlens array to simultaneously capture both conoscopic and orthoscopic views of birefringent objects. *J. Microsc.* **231,** 419–432 (2008).
21. Aarts, D. G. A. L., Schmidt, M. & Lekkerkerker, H. N. W. Direct visual observation of thermal capillary waves. *Science* **304,** 847–850 (2004).
22. Fradin, C. *et al.* Reduction in the surface energy of liquid interfaces at short length scales. *Nature* **403,** 871–874 (2000).
23. Pelcovits, R. A. & Meyer, R. B. Twist penetration in single-layer smectic A discs of colloidal virus particles. *Liq. Cryst.* **36,** 1157–1160 (2009).
24. Kaplan, C. N., Tu, H., Pelcovits, R. A. & Meyer, R. B. Theory of depletion-induced phase transition from chiral smectic-A twisted ribbons to semi-infinite flat membranes. *Phys. Rev. E* **82,** 021701 (2010).
25. Srivastava, S. *et al.* Light-controlled self-assembly of semiconductor nanoparticles into twisted ribbons. *Science* **327,** 1355–1359 (2010).
26. Chung, W. J. *et al.* Biomimetic self-templating supramolecular structures. *Nature* **478,** 364–368 (2011).
27. Grason, G. M. & Bruinsma, R. F. Chirality and equilibrium biopolymer bundles. *Phys. Rev. Lett.* **99,** 098101 (2007).
28. Claessens, M., Semmrich, C., Ramos, L. & Bausch, A. R. Helical twist controls the thickness of F-actin bundles. *Proc. Natl Acad. Sci. USA* **105,** 8819–8822 (2008).
29. Nguyen, T. D. & Glotzer, S. C. Switchable helical structures formed by the hierarchical self-assembly of laterally tethered nanorods. *Small* **5,** 2092–2098 (2009).
30. Nguyen, T. D. & Glotzer, S. C. Reconfigurable assemblies of shape-changing nanorods. *ACS Nano* **4,** 2585–2594 (2010).

Supplementary Information is linked to the online version of the paper at www.nature.com/nature.

Acknowledgements This work was supported by the US National Science Foundation (NSF-MRSEC-0820492, NSF-DMR-0955776, NSF-MRI-0923057, NSF-CMMI-1068566) and the Petroleum Research Fund (ACS-PRF 50558-DNI7). We acknowledge use of the Brandeis MRSEC optical microscopy facility.

Author Contributions T.G., E.B., M.J.Z., R.B.M. and Z.D. designed the experiments and interpreted the results. T.G., E.B. and M.J.Z. performed the experiments. A.W. performed the optical trapping experiments. E.B., C.B. and D.N. performed the electron microscopy imaging. M.H. performed the experiments on mutant viruses. R.O. performed the LC-PolScope imaging. Y.Y. and M.F.H. designed and performed the computer simulations. T.G., E.B., M.J.Z. and Z.D. wrote the manuscript.

Author Information Reprints and permissions information is available at www.nature.com/reprints. The authors declare no competing financial interests. Readers are welcome to comment on the online version of this article at www.nature.com/nature. Correspondence and requests for materials should be addressed to Z.D. (zdogic@brandeis.edu).

METHODS

Virus stock solutions. Filamentous viruses were grown using standard biological techniques that have been discussed elsewhere[31]. The resulting virus suspensions contain a low fraction of multimeric virus particles (dimers and trimers) with longer contour lengths. Because high monodispersity in particle length is essential for assembly of membranes and ribbons, the polydispersity was reduced by fractionating the samples through the isotropic–nematic phase transition, as longer viruses preferentially dissolve in the nematic liquid-crystalline phase. Suspensions of fd viruses (2–8 ml) were prepared at isotropic–nematic phase coexistence. Only the isotropic (top) portion of the sample, enriched in monomeric viruses, was used for subsequent experiments. The fractionation was repeated once or twice to obtain sufficiently monodisperse suspensions that reproducibly assemble into colloidal membranes and ribbons. The polydispersity of virus suspensions was quantified using gel electrophoresis of intact viruses. Approximately 20 µl of a 0.5 mg ml^{-1} virus solution was loaded into a 1.8% agarose gel and run at 1.4 V cm^{-1} for approximately 8 h (ref. 31). The virus coat protein was dissolved by immersing gels in 0.2 M NaOH for 30 min, and the remaining DNA was visualized with ultraviolet light after staining with ethidium bromide[31] (Supplementary Fig. 9). Only virus suspensions with a monodispersity greater than 95% were used for experiments. For florescence microscopy, viruses were labelled with florescent dyes as described previously[32]. The wild-type fd virus was labelled with Alexa 488-NHS ester (Invitrogen) and the Tyr21Met fd virus was labelled with DyLight 546-NHS ester (Pierce). All samples were buffered in 20 mM Tris, pH 8.0, to which 100 mM NaCl was added to screen electrostatic repulsion between viruses. The concentration of the viruses was determined using absorption spectroscopy[13].

Tuning the twist of the cholesteric phase. The strength of chiral interactions between viruses was quantified by measuring the pitch of a cholesteric liquid-crystalline sample. Glass cylindrical capillaries, 0.7 mm in diameter (Charles Supper Company), were filled with fd virus suspensions. For the cholesteric texture to develop properly, it was necessary to clean the capillaries in a hot detergent solution (Hellmanex) after soaking them in 5 M NaOH. After equilibration for several hours, the samples show a well-known fingerprint texture, seen by polarization microscopy, that is characteristic of cholesteric liquid-crystalline phases[13,17] (Supplementary Fig. 1). The twist wavevector, $q_0 = 2\pi/P$, was determined by measuring the cholesteric pitch, P. Bulk samples were prepared at 100 mg ml^{-1}. Previous work, as well as experiments described in Supplementary Fig. 4, indicate that this is the effective virus concentration in membranes and ribbons[11]. We assume that q_0 is the same for bulk cholesteric phase and 2D membranes.

Two complimentary methods were used to tune the strength of chiral interactions between fd viruses: genetic mutations of the major coat protein and physical control of sample temperature. Most aspects of the wild-type fd virus phase behaviour, such as the location of the isotropic–nematic phase transition, are independent of temperature, as is expected for entropic suspensions of hard, rod-like particles. An exception is that the wild-type fd virus persistence length is weakly dependent on temperature[33]. Data shown in Supplementary Fig. 1 indicates that decreasing temperature increases the strength of chiral interactions between the viruses, as evidenced by the measurements of the cholesteric pitch[17]. Notably, the twist wavevector shows evidence of a second-order phase transition from a high-temperature achiral phase to a low-temperature cholesteric phase. By contrast with the temperature-dependent chirality of wild-type fd virus, the chirality of Tyr21Met fd virus does not show any temperature dependence (Supplementary Fig. 6).

An alternative control of chirality involves modifying the composition of the major coat protein. For example, Tyr21Met fd virus, a mutant that differs from wild-type fd virus by a single point mutation of the major coat protein, forms a cholesteric helix with the opposite handedness[13]. By controlling the ratio of wild-type to Tyr21Met fd virus, it is possible to tune the chirality of the resulting suspension[13]. Such mixtures still form colloidal membranes, and fluorescence microscopy indicates that the two components are uniformly dispersed on optically resolvable length scales (~300 nm). We have used both temperature and genetic methods to tune the chirality of the constituent rods.

Light microscopy sample preparation. Light microscopy chambers were assembled using glass slides and coverslips (Goldseal, Fisher Scientific) with a layer of unstretched Parafilm as a spacer. Glass slides and coverslips were coated with an acrylamide brush to prevent non-specific binding of viruses to the glass surfaces, by a procedure described elsewhere[34]. We mixed fd virus with the non-adsorbing polymer Dextran (relative molecular mass, 500,000; Sigma-Aldrich) to from membrane and ribbons samples. The virus concentration remained fixed at 10 mg ml^{-1}, and the Dextran concentration varied between 30 and 50 mg ml^{-1} as indicated in the main text. The samples, sealed using ultraviolet-cured glue (Norland Optical) and stored at 4 °C, remained good for weeks to months.

Optical microscopy. Samples were characterized using a number of complimentary optical microscopy techniques. Except those made using the 3D LC-PolScope, all observations were made using a ×100 oil-immersion objective (Plan Fluor; numerical aperture, 1.3) on an inverted microscope (Nikon TE-2000). Images were recorded with cooled charge-coupled-device (CCD) cameras (CoolSnap HQ, Photometrics, or Retiga Exi, QImaging). The microscope was equipped with traditional polarization optics, a DIC module, a fluorescence imaging module and 2D LC-Polscope microscopy[18]. For 3D PolScope measurements, we used a Zeiss Axiovert 200M microscope with a Plan Apochomat oil-immersion objective (×63; numerical aperture, 1.4) and a monochrome CCD camera[20] (Retiga 4000R, QImaging).

Sample temperature was tuned between 4 and 60 °C with a home-made Peltier module equipped with a proportional–integral–derivative temperature controller (ILX Lightwave LPT 5910). The temperature-controlling side of the Peltier device was attached to a copper ring fitted around the microscope objective, which heats or cools the sample through the immersion oil. A thermistor, placed in the copper ring adjacent to the sample, enabled the proportional–integral–derivative feedback necessary to adjust the temperature. Excess heat was removed using a constant flow of room-temperature water.

3D LC-PolScope microscopy. Membrane edges with left-handed and right-handed twists appear indistinguishable when viewed with 2D LC-PolScope because this technique provides only a 2D projection of the sample birefringence. To determine the 3D orientation of rods, we used 3D LC-PolScope microscopy[20]. The 3D LC-Polscope extends the capabilities of the 2D LC-PolScope by placing a microlens array in the image plane of the objective lens. The microlens array generates a hybrid image consisting of a series of conoscopic microimages, each probing a different spatial area in the image plane. Analysis of each conoscopic microimage reveals the local birefringence as a function of the propagation direction of transmitted light rays. Supplementary Fig. 4a illustrates the path of the optical rays from the specimen plane to the back focal plane of the 3D LC-PolScope microlens array. Rays shown in green and red pass perpendicularly through the membrane, parallel to its optical axis, and experience no differential retardation. Rays shown in black pass at an angle to the optical axis and are differentially retarded. Rays with the same tilt angle in the specimen plane are focused at the same point in the back focal plane of the objective. The array of microlenses, placed in the image plane of the objective, refocuses these rays into a plane behind the microlens array. Behind each microlens, an image of the objective's aperture appears containing multiple conoscopic images, each specific to rays that have passed through a small region of the specimen. For example, rays emanating from the region X of the sample fall onto the microlens X'. Therefore, only rays that passed through X contribute to the conoscopic image behind X'. The same argument applies to rays passing through Y and Y', and so on.

The conoscopic image of a single microlens focused on the bulk portion of the membrane shows a radially symmetric distribution of the retardance that increases away from the centre of the image (Supplementary Fig. 4b). In the centre, the rays of light are aligned with the orientation of the viruses and the retardance is zero. Away from the centre, the retardance increases because the rays of light become tilted with respect to the orientation of the viruses. When the viruses are tilted with respect to the optical axis, for example near the edge of the membrane, the radial profile obtained from a conoscopic image becomes asymmetric and indicates local tilting of the molecules. For colloidal membranes composed of an achiral mixture of wild-type and Tyr21Met fd viruses, the viruses at the edge of a membrane are found to twist in clockwise and anticlockwise directions with equal probability (Supplementary Fig 4c–e).

Analysis of the 3D LC-PolScope retardance profile is used to determine the concentration of viruses within a membrane, because the membrane birefringence is proportional to the local rod concentration. It follows that the local retardance of the membrane is given by $R = \Delta n_{sat} dcS\sin^2(\theta)/\sin(\alpha)$, where θ is the local tilting of the rods, c is the concentration of rods within a membrane, d is the thickness of the colloidal membrane, S is the local order parameter (assumed to be ~1), Δn_{sat} is the specific birefringence of a fully aligned bulk sample of fd virus at unit concentration as determined by X-ray scattering experiments[35] and α is the orientation of the rays of light as a function of the distance, r, to the centre of the conoscopic image. This orientation is given by $\sin(\alpha) = r\mathrm{NA}/r_{\mathrm{NA}}n$, where $r_{\mathrm{NA}} = 3.9$ µm is the size of the conoscopic image, NA = 1.4 is the numerical aperture and $n = 1.33$ is the index of refraction of the solvent. The fitting of this functional form to the retardance profile yields a mean concentration of viruses in the bulk of the membrane of $c = 103 \pm 10$ mg ml^{-1} (Supplementary Fig. 4f). Similar values where obtained by an independent method that involves counting the number of fluorescently labelled particles[11]. Finally, we also note that the concentration of the viruses does not appreciably change with varying Dextran concentration (Supplementary Fig. 4g).

Measurement of the line tension. Line tension was measured by directly imaging and analysing thermal fluctuations of the membrane's edge with DIC optical microscopy using well-established methods[12]. Lower line tension indicates that

less energy is required to place the particles at an interface, resulting in larger fluctuations of the membrane's edge. The conformation of the membrane's edge is described by $h(x)$, the local height of the interface, where x is the lateral position along the interface. The total length of the interface is

$$L = \int \mathrm{d}x \sqrt{1 + \left(\frac{\mathrm{d}h}{\mathrm{d}x}\right)^2} \quad (1)$$

For small fluctuations ($\mathrm{d}h/\mathrm{d}x = \tan(\theta) \approx \theta$), the expression for the excess length of the edge relative to a flat interface can be approximated as

$$\Delta L = \int \mathrm{d}x \sqrt{1+\theta^2} - L \approx \frac{1}{2}\int \mathrm{d}x\, \theta^2(x)$$

If line tension, γ, is the energetic cost per unit length of the edge, the free-energy difference between fluctuating and straight edges is given by $\Delta F = \gamma \Delta L$. Next we decompose $\theta(x)$ into a Fourier series:

$$\theta(x) = \sum\nolimits_q \sqrt{\frac{2}{L}}\, a_q \cos(qx)$$

Here L is the length of the interface and the wavevector, q, is given by $q = n\pi/L$. The energetic cost of the membrane conformation specified by Fourier amplitudes a_q is given by

$$\Delta F = \gamma \Delta L = \frac{\gamma}{2}\int_0^L \mathrm{d}x\, \theta^2(x) = \frac{\gamma}{2}\sum\nolimits_q a_q^2$$

By invoking the equipartition theorem, it is possible to relate the line tension to fluctuations of the interface:

$$\langle a_q^2 \rangle = k_\mathrm{B}T/\gamma \quad (2)$$

To measure $\langle a_q{}^2 \rangle$ experimentally, we acquired a series of uncorrelated images of the interfacial contour. To ensure optimal contrast, the DIC shear axis was always perpendicular to the membrane's edge. Under these conditions, intensity profile cuts taken perpendicular to the edge could be fitted to a Gaussian, yielding the conformation of the edge with subpixel accuracy. Each conformation is described in terms of the Fourier amplitudes, a_q. Averaging over a sufficient number of uncorrelated images yields a fluctuation spectrum as shown in Fig. 2b, where the mean square amplitudes, $\langle a_q{}^2 \rangle$, are plotted as functions of q. In the limit of small q, $\langle a_q{}^2 \rangle$ is independent of wavenumber as predicted by equation (2). As q increases, the fluctuations are suppressed and scale as q^{-2}. The entire fluctuation spectrum can be quantitatively described by the following equation:

$$\langle a_q^2 \rangle = \frac{k_\mathrm{B}T}{\gamma + \kappa q^2} \quad (3)$$

The $1/q^2$ regime can be obtained by including terms that are proportional to the square of the gradient of $\theta(x)$ in equation (1). This indicates that there is a bending energy, κ, associated with fluctuations of the interface, which might be related to the existence of a thin, quasi-1D nematic phase located at the edge of the membrane, where the rods are tilted and the layer's smectic ordering is destroyed.

Laser tweezers. Colloidal membranes and ribbons are easily manipulated using optical tweezers. The laser tweezer set-up was built around an inverted Nikon TE-2000 microscope. A 1,064-nm laser beam (Compass 1064, Coherent) is time-shared between two points by means of a pair of orthogonally oriented paratellurite (TeO_2) acousto-optic deflectors (Intra-Action). The laser is projected onto the back focal plane of an oil-immersion objective (Plan Fluor ×100, NA = 1.3) and subsequently focused onto the imaging plane. Using custom LABVIEW software, multiple trap locations were specified and used to stretch and manipulate membranes and ribbons.

Electron microscopy. For transmission electron microscopy, membranes were assembled as described above but with the following differences. The monolayer membranes are relatively small and only stable in solution; therefore, to keep them intact throughout fixation and staining, we immobilized the membrane assemblies by embedding them in 1% low-melting-temperature agarose (SeaKem; gelation temperature, 25 ± 5 °C), in 100 mM NaCl, 20 mM Tris, pH 8.15, and 150 mM sucrose as a cryoprotectant. Virus samples were mixed in 1.5-ml Eppendorf tubes with fluid agarose at 30 °C and kept warm for 3–6 h to allow formation of relatively large membranes as confirmed by light microscopy. Subsequently, a drop of the fluid sample containing membranes was transferred into the 0.1-mm-high cavity of an aluminium planchette for high-pressure freezing (Wohlwend), which was then closed. Then the sample temperature was decreased to 4 °C for 30–45 min. The gelled samples were rapidly frozen using a Leica HPM-100 high-pressure freezer (Leica Microsystems). Using a Leica AFS-2 device, the frozen samples were freeze-substituted at low temperatures (starting at −90 °C) over the course of three days in a solution containing 1% osmium tetroxide (EMS), 0.5% anhydrous glutaraldehyde (EMS) and 2% water in anhydrous acetone (AC32680-0010, Fisher Scientific). After the temperature was raised to 4 °C, the sample was infiltrated and embedded in EMbed 812-Resin (EMS). Ultrathin, 70-nm, sections were collected on slot grids covered with Formvar support film and post-stained with uranyl acetate (supersaturated solution) and 0.2% lead citrate, before inspection on a FEI Morgan 268 transmission electron microscope with a 1k CCD camera (GATAN) and on a 300-keV Tecnai F30 intermediate-voltage transmission electron microscope (FEI) with a 4k CCD camera (GATAN). For electron tomography, we used 150-nm-thick sections that were coated with 10-nm colloidal gold particles. Tilt series were recorded over an angular range of ±60° with 1° increments on the Tecnai F30 using the microscope control software SERIALEM[36]. Tomographic reconstructions were calculated with the IMOD software using fiducial alignment and weighted back-projection[37].

Computer simulations of the rod/polymer mixture. In the computational model, the rods were represented as hard spherocylinders and the non-adsorbing polymers (depletant) were modelled as ghost spheres, which act as hard spheres when interacting with rods but can freely interpenetrate one another[38]. We performed Metropolis Monte Carlo simulation with periodic boundary conditions. The system contained 6,000 rods in a box with dimensions 140 × 140 × 50 (in units of the rod diameter). A constant osmotic pressure was maintained by coupling ghost spheres to a constant-chemical-potential bath through insertion and deletion moves. The simulations thus sampled the $N_\mathrm{rod}\mu_\mathrm{sphere}VT$ ensemble, where N_rod is the number of rods, μ_sphere is the sphere chemical potential and V is the volume. The rod aspect ratio was 20, the ghost-sphere diameter was 1.5 and on average there were about 520,000 spheres. Simulations were initialized with rods in a monolayer, and Monte Carlo simulation was performed until rod density within the membrane and rod orientations equilibrated. Rods at the membrane edge twisted spontaneously regardless of the initial rod orientations in the membrane.

31. Maniatis, T., Sambrook, J. & Fritsch, E. *Molecular Cloning* Ch. 3 (1989).
32. Lettinga, M. P., Barry, E. & Dogic, Z. Self-diffusion of rod-like viruses in the nematic phase. *Europhys. Lett.* **71,** 692–698 (2005).
33. Tang, J. X. & Fraden, S. Nonmonotonic temperature dependence of the flexibility of bacteriophage fd. *Biopolymers* **39,** 13–22 (1996).
34. Lau, A. W. C., Prasad, A. & Dogic, Z. Condensation of isolated semi-flexible filaments driven by depletion interactions. *Europhys. Lett.* **87,** 48006 (2009).
35. Purdy, K. R. *et al.* Measuring the nematic order of suspensions of colloidal fd virus by X-ray diffraction and optical birefringence. *Phys. Rev. E* **67,** 031708 (2003).
36. Mastronarde, D. N. Automated electron microscope tomography using robust prediction of specimen movements. *J. Struct. Biol.* **152,** 36–51 (2005).
37. Kremer, J. R., Mastronarde, D. N. & McIntosh, J. R. Computer visualization of three-dimensional image data using IMOD. *J. Struct. Biol.* **116,** 71–76 (1996).
38. Yang, Y., Barry, E., Dogic, Z. & Hagan, M. F. Self-assembly of 2D membranes from mixtures of hard rods and depleting polymers. *Soft Matter* **8,** 707–714 (2012).